JACS
JOURNAL OF THE AMERICAN CHEMICAL SOCIETY
Article
Cite This: J. Am. Chem. Soc. 2019, 141, 17610−17616
pubs.acs.org/JACS

Core−Shell ZnO@SnO_2 Nanoparticles for Efficient Inorganic Perovskite Solar Cells

Zhenxing Li,*[,†,∥] Rui Wang,[‡,∥] Jingjing Xue,[‡,∥] Xiaofei Xing,[†] Chengcheng Yu,[†] Tianyi Huang,[‡] Junmei Chu,[†] Kai-Li Wang,[§] Chong Dong,[§] Zhiting Wei,[†] Yepin Zhao,[‡] Zhao-Kui Wang,*[,§] and Yang Yang*[,‡]

[†]State Key Laboratory of Heavy Oil Processing, College of New Energy and Materials, Beijing Key Laboratory of Biogas Upgrading Utilization, China University of Petroleum (Beijing), Beijing 102249, China

[‡]Department of Materials Science and Engineering, University of California, Los Angeles, California 90095, United States

[§]Institute of Functional Nano and Soft Materials (FUNSOM), Jiangsu Key Laboratory for Carbon-Based Functional Materials and Devices, Soochow University, Suzhou, Jiangsu 215123, China

Supporting Information

ABSTRACT: The ideal charge transport materials should exhibit a proper energy level, high carrier mobility, sufficient conductivity, and excellent charge extraction ability. Here, a novel electron transport material was designed and synthesized by using a simple and facile solvothermal method, which is composed of the core−shell ZnO@SnO_2 nanoparticles. Thanks to the good match between the energy level of the SnO_2 shell and the high electron mobility of the core ZnO nanoparticles, the PCE of inorganic perovskite solar cells has reached 14.35% (J_{SC}: 16.45 mA cm^{-2}, V_{OC}: 1.11 V, FF: 79%), acting core−shell ZnO@SnO_2 nanoparticles as the electron transfer layer. The core−shell ZnO@SnO_2 nanoparticles size is 8.1 nm with the SnO_2 shell thickness of 3.4 nm, and the electron mobility is seven times more than SnO_2 nanoparticles. Meanwhile, the uniform core−shell ZnO@SnO_2 nanoparticles is extremely favorable to the growth of inorganic perovskite films. These preliminary results strongly suggest the great potential of this novel electron transfer material in high-efficiency perovskite solar cells.

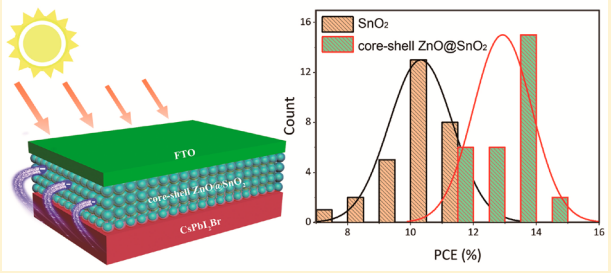

INTRODUCTION

The halide perovskite semiconductors are a fully novel kind of high-efficient, low-cost, and solution processable light-harvesting materials since 2009.[1] The power conversion efficiency (PCE) of perovskite solar cells has already risen to over 22% these years, whose theoretical limit has been estimated to be 31%.[2−9] At present, the perovskite solar cells mostly originated from hybrid inorganic−organic halides, including formamidinium lead halide $FAPbX_3$ methylammonium lead halide $MAPbX_3$ (X= Cl, Br, I) or the mixture of them.[10−16] Because of the volatile organic components, the traditional perovskite solar cells face significant challenges on the thermal stability, which is an obstacle of the long-term practical application.[17−21] The inorganic halide perovskite with chemical formula of $CsPbX_3$ provides an opportunity, which surprisingly keeps stable at a temperature of more than 400 °C without any phase degradation.[22−24] The issues related to the release and decomposition of the organic component in the high temperature can be avoided. Apart from the outstanding thermal stability, the inorganic perovskite, such as α-$CsPbI_3$ perovskite, has 1.73 eV bandgap,[25,26] which is proper to tandem solar cells. The α-$CsPbI_3$ perovskite can combine with either low-bandgap perovskite or silicon,[27−30] whereas α-$CsPbI_3$ perovskite is unstable and transfers spontaneously to the δ-$CsPbI_3$ phase at normal condition. For overcoming the instability of α-$CsPbI_3$, the bromide ion is usually added to reduce phase change temperature from the δ-phase to the α-phase.

The ideal charge transport materials of perovskite solar cells should exhibit a proper energy level, high carrier mobility, adequate conductivity, and excellent charge extraction capacity. At present, the charge transport materials include mainly organic materials such as Spiro-OMeTAD, PTAA, PCBM, and C60 and metal oxide such as SnO_2, TiO_2, ZnO, and NiO_x.[31−40] Compared with the organic charge transport materials, as you know the metal oxides show better stability and field effect mobility than that of organic materials.[41−43] Among these metal oxides, the SnO_2 has been demonstrated to be an efficient electronic transfer layer in inorganic perovskite solar cells[25] because of the appropriate energy level for electron injection of inorganic perovskite. The ZnO shows large electronic mobility (205 cm^2 V^{-1} s^{-1}) on electronic extraction,[44] and the intrinsic surface flaw of the ZnO can easily result in serious surface recombination of electron and hole.[45,46] Additionally, the perovskite crystals can be easily

Received: June 26, 2019
Published: October 22, 2019

DOI: 10.1021/jacs.9b06796
J. Am. Chem. Soc. 2019, 141, 17610−17616

decomposed during thermal treatment, when the ZnO directly contacts with the perovskite crystals, because of the generated hydroxide constitutions on the surface of ZnO.[47,48] Hence, the core−shell ZnO@SnO_2 nanoparticles, combining the advantage of SnO_2 and ZnO, is an ideal electron transport layer, where the shell SnO_2 provides a matched energy level alignment for electron injection, and the core ZnO nanoparticles provide a high electron mobility. Herein, we design and synthesize the core−shell ZnO@SnO_2 nanoparticles by using a simple and facile solvothermal method, which can act as an electronic transfer medium inside the inorganic perovskite solar cells. And the core−shell ZnO@SnO_2 nanoparticles is 8.1 nm, and the core ZnO nanoparticle is 4.7 nm, and the shell thickness is 3.4 nm. Contrast with SnO_2 nanoparticles, the novel electron transport material could remarkably increase efficiency on inorganic perovskite solar cells because of good matching between the energy level and the high electron mobility of core ZnO nanoparticles. The $CsPbI_2Br$ solar cells with the core−shell ZnO@SnO_2 nanoparticles serving as an electron transport layer exhibit a high PCE of 14.35%. Our preliminary results indicate the great potential of this novel electronic transfer material on the high-efficiency perovskite solar cell.

EXPERIMENTAL SECTION

Materials. Zinc acetate ($Zn(CH_3COO)_2$, 99.999%) and tin(IV) acetate ($Sn(CH_3COO)_4$) power were purchased from Sigma-Aldrich. Lead iodide (PbI_2, 99.999%), lead bromide ($PbBr_2$, 99.999%), barium iodide (CsI, 99.99%), and barium bromide (CsBr, 99.99%) power was bought at Alfa Aesar. N,N-Dimethylformamide (DMF, 99.9%) was bought at Alfa Aesar. And the company of 1-Material Ltd. provided Spiro-OMeTAD. SnO_2 nanoparticles colloid dispersion (tin(IV) oxide) were obtained from Alfa Aesar. And the whole materials were used without other purification processes.

Synthesis of Core−Shell ZnO@SnO_2 Nanoparticles. Zinc acetate (0.21 g) and 75 μL of H_2O were dispersed into methanol (10 mL) under stirring at 62 °C. Then, a 0.43 mol L^{-1} of KOH solution (5 mL) in methanol was dropped at 62 °C. The miscible liquid was blended for 4 h at 62 °C. Then the obtained white sediment was cleaned with methanol for three times. After that, a 0.05 mol L^{-1} solution of tin(IV) acetate (20 mL) in methanol and 75 μL of H_2O were dropped. This reaction mixture continued to stir for 3 h at room temperature and 2.5 h at 62 °C to obtain the core−shell ZnO@SnO_2 nanoparticles. The core−shell ZnO@SnO_2 nanoparticles was washed with methanol three times and then redispersed in 10 mg mL^{-1} of chloroform.

Solution Preparation. $CsPbI_2Br$ precursor solution: the solution obtained by adding CsI:CsBr:PbI_2:$PbBr_2$ (1:0.5:1:0.5) in dimethyl sulfoxide (DMSO) into 0.8 M in a N_2 glovebox and dissolved by stirring at 55 °C for 1 h. The reaction mixture was made by adding Sprio-OMeTAD (90 mg), sufonyl imide (Li-TFSI, 22.5 μL) solution (520 mg Li-TFSI in 1 mL acetonitrile), and *tert*-butylpyidine (tBP, 36 μL) in chlorbenzene (CB) solution (1 mL). Then, the liquid was stirred within 24 h under 60 °C.

Device Fabrication. The acetone, ethanol, and deionized water were separately utilized to wash the FTO (15 Ω sq^{-1}) substrates accompanying ultrasonic within 10 min. After that, the core−shell ZnO@SnO_2 nanoparticles solution (10 mg mL^{-1}) or SnO_2 nanoparticles colloid solution (10 mg mL^{-1}) were spin-coated to the washed FTO substrate at 5000 rpm within 30 s, and the prepared films were calcined at 180 °C within 40 min. The substrates were cooled down in air. Then the perovskite precursor liquor was spin-coated at 1000 and 4000 rpm for 20 and 40 s. In the second spin-coating step, the substrate was treated by chlorobenzene drop-casting. Particularly, the substrates were carried out using an annealing process at 260 °C for 10 min. Then the perovskite layer was loaded with HTL at 5000 rpm within 40 s. Lastly, those substrates were moved into a vacuum under 2×10^{-6} Torr to facilitate the evaporation process of MoO_3 (8 nm) and the Ag (100 nm) electrode (metal mask with an aperture area of 0.09 cm^2).

Characterization. The transmission electron microscopy (TEM) images were taken on JEM 2100 LaB6 at 200 kV. The high-resolution transmission electron microscope (HRTEM), line scan profiles, and energy-dispersive spectrometry (EDS) mapping were all operated on Tecnai F20 at 200 kV. The SEM images were obtained through Hitachi SU8010 (Japan) at 200 kV. The wide-angle X-ray diffraction (XRD) analysis was characterized with a Burker D8-advance X-ray power diffractometer at 40 kV and 40 mA. X-ray photoelectron spectrometer (XPS) was handled with an ion-pumped chamber (evacuated to 2×10^{-9} Torr). UV−vis absorption spectrum was collected through U-4100 spectrophotometer (Hitachi) with an integrating sphere. The perovskite layer was coated on an ITO substrate for the measurements. The work function of samples and the position of the maximum value of valence bands were ascertained by ultraviolet photoelectron spectroscopy (UPS). Excitation was performed using a He discharge lamp capable of emitting ultraviolet energy at 21.2 eV. The entire UPS measurement was done using a standard program with a −7 V bias applied between the sample and the detector. Here, pure gold played a role in the reference.

Device Characterization. Keithley 2400 source meter provided the current density−voltage (*J-V*) curves of inorganic perovskite solar cells; in particular, a light intensity was calibrated according to the silicon solar cell 91150. AFM images were received through the Veeco Multimode to assess surface appearance of films. And the calculated steady-state power conversion efficiency can be received through measuring the stable photocurrent density at a constant bias voltage. For transient photovoltage (TPV) and current (TPC) measurements, the white light bias is triggered by Molex 180081−4320, imitating the operating conditions of a 0.5 solar bias light. The perturbation hypothesis of the excitation light is established by controlling the intensity of the perturbed laser pulse to keep the amplitude of the transient V_{OC} that was less than 5 mV. Measurements were made on an open-circuit voltage and short-circuit current on 50 Ω and 1 MΩ resistors and collected through a digital oscilloscope.

RESULTS AND DISCUSSION

These core−shell ZnO@SnO_2 nanoparticles are prepared via a simple and facile solvothermal means, which employs a methanol serving solvent. First, this core ZnO nanoparticle is obtained in methanol solution by hydrolysis and condensation of zinc acetate with potassium hydroxide.[49] Then, the tin(IV) acetate and water are added into the methanol solution, and the shell SnO_2 is grown on the core ZnO nanoparticles by hydrolysis and condensation of tin(IV) acetate. Figure 1 demonstrates the synthetic strategy of core−shell ZnO@SnO_2 nanoparticles.

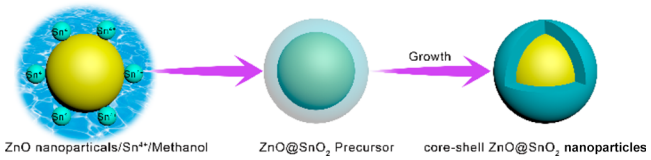

Figure 1. Synthetic diagram of core−shell ZnO@SnO_2 nanoparticles.

Figure 2a displays the TEM photo of core−shell ZnO@SnO_2 nanoparticles, with an average nanoparticle size of 8.1 nm. The clear core−shell ZnO@SnO_2 nanoparticles are shown in high-resolution TEM (HRTEM) (Figure 2b), and the core of this nanoparticles is 4.7 nm. In addition, the shell thickness is 3.4 nm. An apparent lattice spacing of 0.28 nm in the core corresponds to the (100) facets of hexagonal phase ZnO, while the lattice spacing of 0.26 nm in this shell corresponds to the

DOI: 10.1021/jacs.9b06796
J. Am. Chem. Soc. 2019, 141, 17610−17616

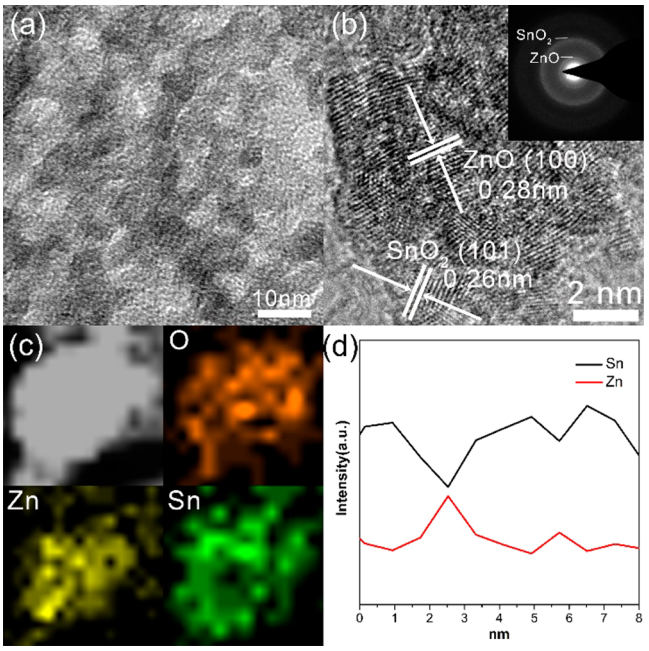

Figure 2. (a) TEM and (b) HRTEM image of core–shell ZnO@SnO_2 nanoparticles; (c) EDS elemental mappings of core–shell ZnO@SnO_2 nanoparticles; and (d) line scan analysis of core–shell ZnO@SnO_2 nanoparticles.

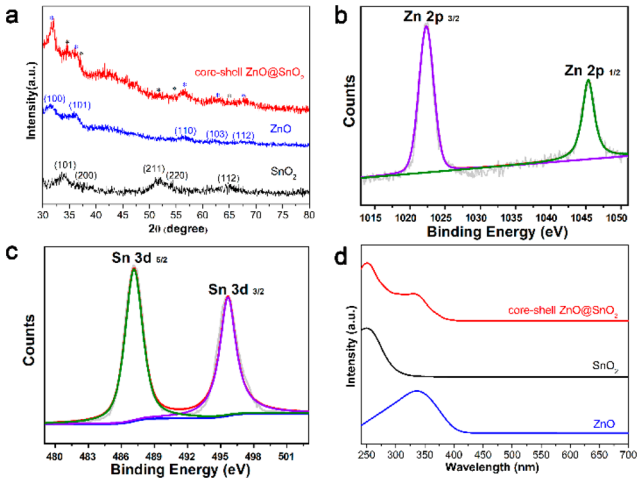

Figure 3. (a) XRD of ZnO, SnO_2, and core–shell ZnO@SnO_2 nanoparticles; XPS of (b) Zn 2p and (c) Sn 3d (the * represents the peaks); and (d) UV–vis absorption spectra of ZnO nanoparticles, SnO_2 nanoparticles, and core–shell ZnO@SnO_2 nanoparticles.

(110) facets of the tetragonal phase SnO_2. In addition, the SAED pattern exhibits diffractions of ZnO and SnO_2 (inset in Figure 2b), and the SAED rings suggest (100) facets of ZnO and (110) facets of SnO_2, respectively. Further, as displayed in Figure 2c, the core–shell ZnO@SnO_2 nanoparticles are also confirmed through the relevant HAADF-STEM pattern. The elemental mappings (Figure 2c) and line scan profiles (Figure 2d) of core–shell ZnO@SnO_2 nanoparticles are finished by EDS for Zn, O, and Sn. Obviously, the Zn is mainly distributed in the center of the nanoparticles and the Sn is mainly distributed in the center of the particles, while the O is uniformly distributed throughout the nanoparticles, which corresponds to the previous results of HRTEM. The data strongly confirms that the process of core–shell ZnO@SnO_2 nanoparticles is dependable. The EDS analysis shows that the ratio of Zn:Sn:O is 16:21:63 (Figure S1, Figure S2, and Table S1).

The crystal phase and composition of ZnO, SnO_2, and ZnO@SnO_2 nanoparticles are detected through powder X-ray diffraction (XRD), obviously disclosing that core–shell ZnO@SnO_2 nanoparticles are obtained. Figure 3a shows the XRD of ZnO nanoparticles, SnO_2 nanoparticles, and core–shell ZnO@SnO_2 nanoparticles. The diffraction peak position and relative intensity of core–shell ZnO@SnO_2 nanoparticles corresponding to standard diffraction data of ZnO and SnO_2 (JCPDS card nos. 36-1451 and 41-1445). The 2θ peaks at 36.4° and 43.3° correspond to the (111) facet of ZnO, and the peaks at correspond to the (111) facet of SnO_2. Therefore, the nanoparticles are the combination of ZnO and SnO_2. The X-ray photoelectron spectroscopy (XPS) of core–shell ZnO@SnO_2 nanoparticles is performed to understand the surface chemical structure. Figure 3 clearly reveals XPS spectra of Zn 2p and Sn 3d. Detailed XPS survey spectra of Zn 2p and Sn 3d are shown in Figure 3b,c. For the Zn 2p region, two characteristic peaks at ~1022.3 and ~1045.3 eV are attributed to the $2p_{3/2}$ and $2p_{1/2}$ of the Zn^{2+} state, with a spin–orbit splitting energy of 23 eV. The Sn 3d peaks are observed at the positions of 487.8 eV ($3d_{5/2}$) and 496.1 eV ($3d_{3/2}$) with a spin–orbit splitting energy of 8.3 eV, respectively, which belong to the Sn^{4+} state.[50] The O 1s peak is observed at the positions of 531.8 eV (Figure S3a), which are assigned to the O^{2-} state, and the XPS spectra of core–shell ZnO@SnO_2 nanoparticles is observed in Figure S3b.

For the purpose of revealing the bandgap energy of core–shell ZnO@SnO_2 nanoparticles, the UV–vis absorption spectra of ZnO nanoparticles, SnO_2 nanoparticles, and core–shell ZnO@SnO_2 nanoparticles are recorded in Figure 3d. The absorption peaks of ZnO and SnO_2 nanoparticles are located around 336.3 and 249.3 nm, which contribute to band gap energies of 3.28 eV (Figure S4a) and 3.46 eV (Figure S4b), respectively. The values are very close to the reported values of ZnO (3.37 eV) and SnO_2 (3.5 eV).[51,52] For core–shell ZnO@SnO_2 nanoparticles, it is obvious that there are two absorption peaks at 335.8 and 250.2 nm, respectively. The former is assigned to the characteristic absorption of ZnO, and the latter is assigned to the SnO_2 nanoparticles. The appearance of two characteristic absorption peaks further confirms that the core–shell ZnO@SnO_2 nanoparticles are composed by ZnO and SnO_2. Obviously, the absorption intensity of SnO_2 is much larger than that of ZnO, indicating that ZnO is coated with SnO_2.

The electronic structure of the valence band of core–shell ZnO@SnO_2 nanoparticles is investigated by using the ultraviolet photoemission spectroscopy (UPS) (He I light), as presented in Figure 4a,b. The valence band maximum (VBM) lies in 3.45 eV below Fermi level, which is explained through simulating a straight line into the leading edge. The second electronic onset is 16.83 eV (Figure 4b) on the left side of the spectrum. The calculated work function is 4.37 eV by subtracting the second electronic onset position of the UPS spectrum from the excitation energy (21.2 eV). Considering that the bandgap energy is 3.43 eV, the energy level of the conduction band minimum (CBM) can be calculated as 4.39 eV. Similarly, the bandgap energy is 3.46 eV and the secondary electron onset is 16.79 eV (Figure 4c,d); the CBM of SnO_2 nanoparticles can be calculated as 4.43 eV. Compared with the

DOI: 10.1021/jacs.9b06796
J. Am. Chem. Soc. 2019, 141, 17610–17616

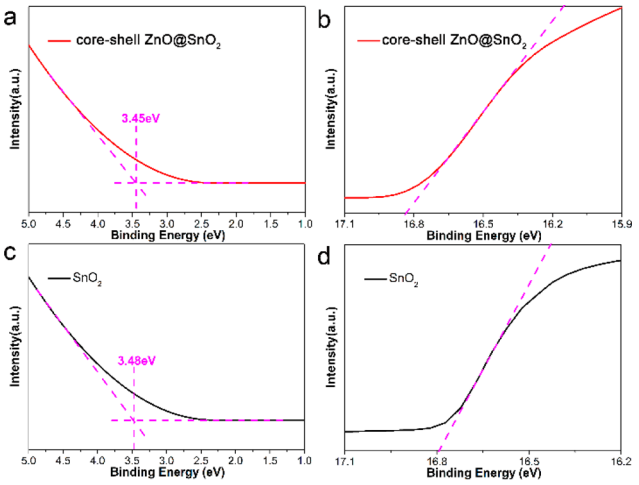

Figure 4. Valence bands and secondary electron cutoff regions of (a, b) core−shell ZnO@SnO_2 nanoparticles and (c, d) SnO_2 nanoparticles by ultraviolet photoemission spectroscopy.

SnO_2 nanoparticles, the core−shell ZnO@SnO_2 nanoparticles match better with the energy level of $CsPbI_2Br$ (4.17 eV) calculated from Figure S5. On the basis of the energy level alignment theory, which can effectively promote electronic transition and lower the possibility of charge recombination of perovskite, facilitating higher open-circuit voltage (V_{OC}) of solar cells.

The morphological influence of core−shell ZnO@SnO_2 nanoparticles on inorganic perovskite was also studied. The SEM image of inorganic perovskite on the core−shell ZnO@SnO_2 nanoparticles and SnO_2 nanoparticles is shown in Figure 5, and the surface morphology of inorganic perovskite exhibited a significant difference. The grain size range on the core−shell ZnO@SnO_2 nanoparticles was 100−200 nm, and

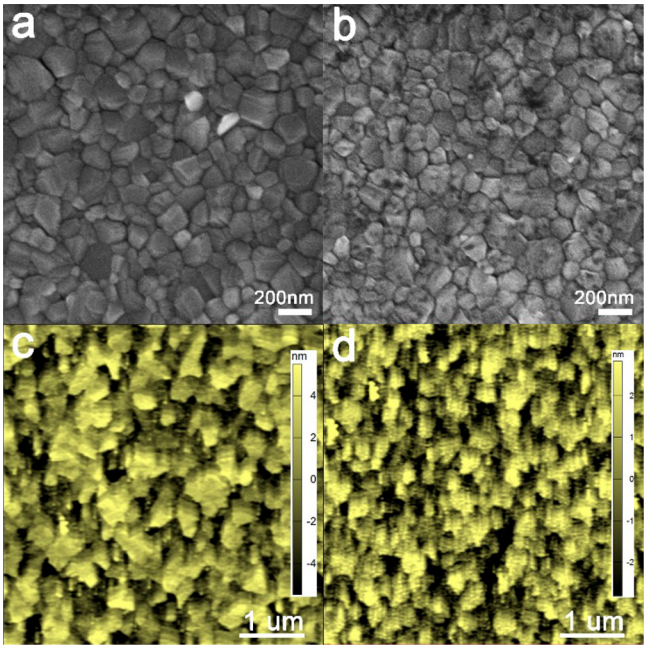

Figure 5. SEM image of inorganic perovskite on the (a) core−shell ZnO@SnO_2 nanoparticles and (b) SnO_2 nanoparticles; AFM of the (c) core−shell ZnO@SnO_2 nanoparticles film and (d) SnO_2 nanoparticles film.

the grain surface was smooth without any defects; the grain size on the SnO_2 nanoparticles was smaller (50−100 nm), and the grain surface was rough with many defects. In order to deeply understand the effect of ZnO@SnO_2 nanoparticles on inorganic perovskite, the morphology of ZnO@SnO_2 nanoparticles and SnO_2 nanoparticles thin film is observed through AFM in Figure 5c,d. Because of uniform particle size, the core−shell ZnO@SnO_2 nanoparticles thin film was more contiguous and smoother than SnO_2 nanoparticles. On the basis of the above experimental results, the core−shell ZnO@SnO_2 nanoparticles are considered an excellent electron transport layer.

The schematic of the device structure of inorganic perovskite solar cell along with relevant SEM cross-section image is presented in Figure 6, and the schematic band energy

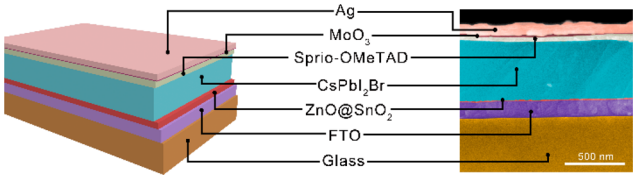

Figure 6. Schematic of the device structure of the inorganic perovskite solar cell.

diagram of the inorganic perovskite solar cell is presented in Figure S6. It includes the glass/FTO/ZnO@SnO_2/perovskite ($CsPbI_2Br$)/Sprio-OMeTAD/MoO_3/Ag, where the core−shell ZnO@SnO_2 nanoparticles act as the electronic transfer layer (ETL). The corresponding current density-open voltage ($J-V$) curves of the optimized device employing the core−shell ZnO@SnO_2 nanoparticles device and SnO_2 nanoparticles device are presented in Figure 7a. The highest PCE reaches up to 14.35%, the short-circuit current (J_{SC}) was 16.45 mA/cm^2, the V_{OC} was 1.11 V, and the fill factor (FF) is 79%. While the PCE of reference device with SnO_2 nanoparticles serving as

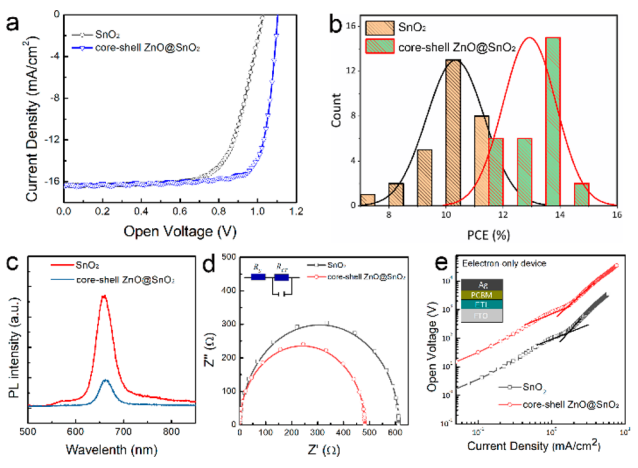

Figure 7. (a) Current density-voltage (J-V) characteristics of the inorganic perovskite solar cells based on different electron transport layer under AM 1.5G illumination with a light intensity of 100 mW/cm^2; (b) PCE distribution of over 30 devices; (c) PL spectra of the $CsPbI_2Br$ film based on different electron transport layer; (d) Nyquist plots of the core−shell ZnO@SnO_2 nanoparticles and SnO_2 nanoparticles; and (e) voltage-current density (V-J) characteristics of the electron-only devices with the FTO/ETL(80 nm)/PCBM/Ag structure.

DOI: 10.1021/jacs.9b06796
J. Am. Chem. Soc. 2019, 141, 17610−17616

electron transport layer was 11.66%, the J_{SC}, V_{OC}, and FF is 16.34 mA/cm^2, 1.03 V, and 69%, respectively. The parameters are shown in Table 1. It is worth noting that the V_{OC} with

Table 1. Photovoltaic Performance of the Core-Shell ZnO@SnO_2 Nanoparticles Device and SnO_2 Nanoparticles Device from *J*−*V* Measurements

device	V_{OC} (V)	J_{SC} (mA/cm^2)	FF (%)	PCE (%)
SnO_2 nanoparticles	1.03	16.34	0.69	11.66
core−shell ZnO@SnO_2 nanoparticles	1.11	16.45	0.79	14.35

core−shell ZnO@SnO_2 nanoparticles is much higher than the SnO_2 nanoparticles, which is put down to excellent energy alignment and higher electron mobility of ZnO, increasing electrons extraction and decreasing nonradiative recombination sites. The device with PCE of over 14% can be highly reproducible with an optimized process, and a statistical PCE distribution on over 30 devices is proven in Figure 7b, while the PCE distribution of the reference device is mainly concentrated in 10%. The shelf stability was also compared, the device of ZnO@SnO_2 having better stability than SnO_2 (Figure S7). The steady-state photoluminescence (PL) was utilized to study the electronic transfer dynamic between the core−shell ZnO@SnO_2 nanoparticles and $CsPbI_2Br$ films. The steady-state PL spectra of the $CsPbI_2Br$ film using the core−shell ZnO@SnO_2 nanoparticles and SnO_2 nanoparticles as electronic transfer layer on FTO/glass substrates are shown in Figure 7c. The PL of the $CsPbI_2Br$ film with core−shell ZnO@SnO_2 nanoparticles as electron transport layer was less than one-third of the SnO_2 nanoparticles, indicating a stronger PL quenching effect of ZnO@SnO_2 nanoparticles. On the basis of above results, the core−shell ZnO@SnO_2 nanoparticles coated on $CsPbI_2Br$ film could extract electron carriers more effectively, which is in perfect accordance with the larger FF. Meanwhile, the electron transfer properties of core−shell ZnO@SnO_2 nanoparticles and SnO_2 nanoparticles were studied by electrochemical impedance spectroscopy (EIS) in Figure 7d, and core−shell ZnO@SnO_2 nanoparticles showed a smaller diameter of semicircle than SnO_2 nanoparticles. The equivalent circuit diagram was a parallel circuit, including charge transfer resistance (R_{CT}) and series resistance (R_s). R_s of core−shell ZnO@SnO_2 nanoparticles was 241 Ω, while R_s of SnO_2 nanoparticles was 305 Ω (Table S2), which indicates that the electrons could be extracted and transported more effectively in the core−shell ZnO@SnO_2 nanoparticles. The electron mobility of core−shell ZnO@SnO_2 nanoparticles was assessed via open voltage−current density (*J*−*V*) curves of the electron-only devices in Figure 7e, and the relevant device structure FTO/ETL(80 nm)/PCBM/Ag was used. The space charge limited current (SCLC) model with eq 1 was used to obtain electron mobility (μ).

$$J = 9/8\varepsilon_0\varepsilon_r\mu V^2/d^3 \quad (1)$$

where ε_0 is the permittivity of free space (8.8542 × 10^{-14} F cm^{-1}), ε_r is the relative dielectric constant of the core−shell ZnO@SnO_2 nanoparticles film (12.5), d is the film thickness (80 nm). The calculated electron mobility is summarized in Table S3. And it is noteworthy to point out that the electron mobility of core−shell ZnO@SnO_2 nanoparticles (0.197 cm^2 V^{-1} s^{-1}) was seven times more than SnO_2 nanoparticles (0.0279 cm^2 V^{-1} s^{-1}) because of high electronic mobility of core ZnO nanoparticles. The electron concentration (n_e) of core−shell ZnO@SnO_2 nanoparticles and SnO_2 nanoparticles were 4.13 × 10^{18} cm^{-3} and 4.50 × 10^{18} cm^{-3}, respectively.

The charge carrier lifetime and extraction ability of the perovskite and electron transport layer interface are studied by using the transient photocurrent (TPC) and transient photovoltage (TPV) decay, respectively, in Figure 8. Single

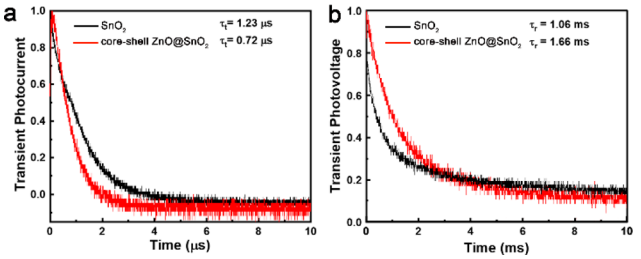

Figure 8. TPC and TPV measurements of the core−shell ZnO@SnO_2 nanoparticles device and SnO_2 nanoparticles device.

exponential decay model was utilized to fit the curves. Figure 8a shows the TPC decay under short-circuit for the core−shell ZnO@SnO_2 nanoparticles device and SnO_2 nanoparticles device. The photocurrent decay time of core−shell ZnO@SnO_2 nanoparticles device (0.72 μs) decreases a lot, compared with the SnO_2 nanoparticles device (1.23 μs). The faster decay profile indicated the better charge extraction efficiency of the device on the basis of ZnO@SnO_2 nanoparticles compared with the SnO_2 nanoparticle device. TPV decay was operated under an open-circuit condition, and the photovoltage decay time in a core−shell ZnO@SnO_2 nanoparticles device is 1.66 ms (Figure 8b), which is much longer than that observed in the SnO_2 nanoparticles device (1.06 ms). The decrease of the generation of photovoltage is because of a recombination of holes and electrons, which confirms that core−shell ZnO@SnO_2 nanoparticles are beneficial to reduce the unwanted nonradiative recombination process.[53] Because of the energy level matching, the core−shell ZnO@SnO_2 nanoparticles device shows a better electron extraction capability and reduces the extraction time.

CONCLUSIONS

In summary, we design and synthesize an outstanding electronic transfer layer for the perovskite solar cells, which are composed of core−shell ZnO@SnO_2 nanoparticles. The core−shell ZnO@SnO_2 nanoparticles was prepared by using a simple and facile solvothermal method, and the particle size is 8.1 nm, with the SnO_2 shell thickness of 3.4 nm. Compared with the SnO_2 nanoparticles, this novel electron transport material improves greatly the efficiency of inorganic perovskite solar cells, which could be put down as well matched between the energy level and high electron mobility of core ZnO nanoparticles. The $CsPbI_2Br$ solar cells with the core−shell ZnO@SnO_2 nanoparticles as electron transport layer exhibit a high PCE of 14.35%. We make sure that the preliminary results indicate a great potential of these novel electron transport materials in highly stable and efficient perovskite solar cells.

DOI: 10.1021/jacs.9b06796
J. Am. Chem. Soc. 2019, 141, 17610−17616

■ ASSOCIATED CONTENT

Supporting Information

The Supporting Information is available free of charge on the ACS Publications website at DOI: 10.1021/jacs.9b06796.

EDS and XPS of ZnO@SnO_2 nanoparticles, the band gap energies of ZnO and SnO_2, the valence bands and secondary electron cutoff regions of $CsPbI_2Br$, EIS of the core−shell ZnO@SnO_2 nanoparticles and SnO_2 nanoparticles, and the schematic band energy diagram of the inorganic perovskite solar cell (PDF)

■ AUTHOR INFORMATION

Corresponding Authors

*lizx@cup.edu.cn
*zkwang@suda.edu.cn
*yangy@ucla.edu

ORCID

Zhenxing Li: 0000-0002-4020-7490
Zhao-Kui Wang: 0000-0003-1707-499X
Yang Yang: 0000-0001-8833-7641

Author Contributions

‖Z.L., R.W., and J.X. contributed equally to this paper.

Notes

The authors declare no competing financial interest.

■ ACKNOWLEDGMENTS

We gratefully acknowledge the Natural Science Foundation of China (no. 61674109), the National Key Research and Development Program of China (no. 2016YFA0202402), the Natural Science Foundation of Jiangsu Province (no. BK20170059), financial support from the Beijing Natural Science Foundation (2182061) (Z.L.), Science Foundation of China University of Petroleum, Beijing (2462019BJRC001) (Z.L.), Air Force Office of Scientific Research (AFOSR) (FA2386-15-1-4108) (Y.Y.), Office of Naval Research (ONR) (N00014-14-181-0648) (Y.Y.), National Science Foundation (NSF) (ECCS-1509955) (Y.Y.), and UC-Solar Program (MRPI 328368) (Y.Y.). This project is also funded by the Collaborative Innovation Center of Suzhou Nano Science and Technology, the Priority Academic Program Development of Jiangsu Higher Education Institutions (PAPD), and by the "111" Project of The State Administration of Foreign Experts Affairs of China.

■ REFERENCES

(1) Kojima, A.; Teshima, K.; Shirai, Y.; Miyasaka, T. Organometal halide perovskites as visible-light sensitizers for photovoltaic cells. *J. Am. Chem. Soc.* **2009**, *131*, 6050.

(2) Huang, J.; Yuan, Y.; Shao, Y.; Yan, Y. Understanding the physical properties of hybrid perovskites for photovoltaic applications. *Nat. Rev. Mater.* **2017**, *2*, 17042.

(3) Zhao, Y.; Zhu, K. Organic-inorganic hybrid lead halide perovskites for optoelectronic and electronic applications. *Chem. Soc. Rev.* **2016**, *45*, 655.

(4) Liu, M.; Johnston, M. B.; Snaith, H. J. Efficient planar heterojunction perovskite solar cells by vapour deposition. *Nature* **2013**, *501*, 395.

(5) Lee, M. M.; Teuscher, J.; Miyasaka, T.; Murakami, T. N.; Snaith, H. J. Efficient hybrid solar cells based on meso-superstructured organometal halide perovskites. *Science* **2012**, *338*, 643.

(6) Kim, H.-S.; Lee, C.-R.; Im, J.-H.; Lee, K.-B.; Moehl, T.; Marchioro, A.; Moon, S.-J.; Humphry-Baker, R.; Yum, J.-H.; Moser, J. E.; Gratzel, M.; Park, N.-G. Lead iodide perovskite sensitized all-solid-state submicron thin film mesoscopic solar cell with efficiency exceeding 9%. *Sci. Rep.* **2012**, *2*, 591.

(7) Zhou, H.; Chen, Q.; Li, G.; Luo, S.; Song, T. B.; Duan, H. S.; Hong, Z.; You, J.; Liu, Y.; Yang, Y. Photovoltaics. Interface engineering of highly efficient perovskite solar cells. *Science* **2014**, *345*, 542.

(8) Yang, W. S.; Noh, J. H.; Jeon, N. J.; Kim, Y. C.; Ryu, S.; Seo, J.; Seok, S. I. High-performance photovoltaic perovskite layers fabricated through intramolecular exchange. *Science* **2015**, *348*, 1234.

(9) Kaltenbrunner, M.; Adam, G.; Glowacki, E. D.; Drack, M.; Schwodiauer, R.; Leonat, L.; Apaydin, D. H.; Groiss, H.; Scharber, M. C.; White, M. S.; Sariciftci, N. S.; Bauer, S. Flexible high power-per-weight perovskite solar cells with chromium oxide-metal contacts for improved stability in air. *Nat. Mater.* **2015**, *14*, 1032.

(10) Shao, Y.; Yuan, Y.; Huang, J. Correlation of energy disorder and open-circuit voltage in hybrid perovskite solar cells. *Nat. Energy* **2016**, *1*, 15001.

(11) You, J.; Meng, L.; Song, T. B.; Guo, T.-F.; Yang, Y.; Chang, W.-H.; Hong, Z.; Chen, H.; Zhou, H.; Chen, Q.; Liu, Y.; De Marco, N.; Yang, Y. Improved air stability of perovskite solar cells via solution-processed metal oxide transport layers. *Nat. Nanotechnol.* **2016**, *11*, 75.

(12) Nie, W.; Tsai, H.; Asadpour, R.; Blancon, J. C.; Neukirch, A. J.; Gupta, G.; Crochet, J. J.; Chhowalla, M.; Tretiak, S.; Alam, M. A.; Wang, H. L.; Mohite, A. D. High-efficiency solution-processed perovskite solar cells with millimeter-scale grains. *Science* **2015**, *347*, 522.

(13) Jeon, N. J.; Noh, J. H.; Yang, W. S.; Kim, Y. C.; Ryu, S.; Seo, J.; Seok, S. I. Compositional engineering of perovskite materials for high-performance solar cells. *Nature* **2015**, *517*, 476.

(14) Son, D. Y.; Lee, J. W.; Choi, Y. J.; Jang, I. H.; Lee, S.; Yoo, P. J.; Shin, H.; Ahn, N.; Choi, M.; Kim, D.; Park, N. G. Self-formed grain boundary healing layer for highly efficient $CH_3NH_3PbI_3$ perovskite solar cells. *Nat. Energy* **2016**, *1*, 16081.

(15) Jiang, Q.; Zhang, L. Q.; Wang, H. L.; Yang, X. L.; Meng, J. H.; Liu, H.; Yin, Z. G.; Wu, J. L.; Zhang, X. W.; You, J. B. Enhanced electron extraction using SnO_2 for high-efficiency planar-structure $HC(NH_2)_2PbI_3$-based perovskite solar cells. *Nat. Energy* **2017**, *2*, 16177.

(16) Tan, H.; Jain, A.; Voznyy, O.; Lan, X.; Garcia de Arquer, F. P.; Fan, J. Z.; Quintero-Bermudez, R.; Yuan, M.; Zhang, B.; Zhao, Y.; Fan, F.; Li, P.; Quan, L. N.; Zhao, Y.; Lu, Z. H.; Yang, Z.; Hoogland, S.; Sargent, E. H. Efficient and stable solution-processed planar perovskite solar cells via contact passivation. *Science* **2017**, *355*, 722.

(17) Li, M.; Zhao, C.; Wang, Z.-K.; Zhang, C.-C.; Lee, H. K. H.; Pockett, A.; Barbe, J.; Tsoi, W. C.; Yang, Y.-G.; Carnie, M. J.; Gao, X.-Y.; Yang, W.-X.; Durrant, J. R.; Liao, L.-S.; Jain, S. M. Interface modification by ionic liquid: a promising candidate for indoor light harvesting and stability improvement of planar perovskite solar cells. *Adv. Energy Mater.* **2018**, *8*, 1801509.

(18) Conings, B.; Drijkoningen, J.; Gauquelin, N.; Babayigit, A.; D'Haen, J.; D'Olieslaeger, L.; Ethirajan, A.; Verbeeck, J.; Manca, J.; Mosconi, E.; Angelis, F. D.; Boyen, H.-G. Intrinsic thermal instability of methylammonium lead trihalide perovskite. *Adv. Energy Mater.* **2015**, *5*, 1500477.

(19) Xue, J.; Wang, R.; Wang, K. L.; Wang, Z. K.; Yavuz, I.; Wang, Y.; Yang, Y.; Gao, X.; Huang, T.; Nuryyeva, S.; Lee, J. W.; Duan, Y.; Liao, L. S.; Kaner, R.; Yang, Y. Crystalline Liquid-like Behavior: Surface-Induced Secondary Grain Growth of Photovoltaic Perovskite Thin Film. *J. Am. Chem. Soc.* **2019**, *141*, 13948.

(20) Wang, R.; Mujahid, M.; Duan, Y.; Wang, Z. K.; Xue, J.; Yang, Y. A Review of Perovskites Solar Cell Stability. *Adv. Funct. Mater.* **2019**, 1808843.

(21) Wang, R.; Xue, J.; Meng, L.; Lee, J.-W.; Zhao, Z.; Sun, P.; Cai, L.; Huang, T.; Wang, Z.; Wang, Z.-K.; Duan, Y.; Yang, J. L.; Tan, S.; Yuan, Y.; Huang, Y.; Yang, Y. Caffeine Improves the Performance and Thermal Stability of Perovskite Solar Cells. *Joule* **2019**, *3*, 1464.

DOI: 10.1021/jacs.9b06796
J. Am. Chem. Soc. 2019, 141, 17610−17616

(22) Wang, P. Y.; Zhang, X. W.; Zhou, Y. Q.; Jiang, Q.; Ye, Q. F.; Chu, Z. M.; Li, X. X.; Yang, X. L.; Yin, Z. G.; You, J. Solvent-controlled growth of inorganic perovskite films in dry environment for efficient and stable solar cells. *Nat. Commun.* **2018**, *9*, 2225.
(23) Wang, K.; Wang, R.; Wang, Z.; Li, M.; Zhang, Y.; Ma, H.; Liao, L.; Yang, Y. Tailored Phase Transformation of $CsPbI_2Br$ Films by Copper(II) Bromide for High-Performance All-Inorganic Perovskite Solar Cells. *Nano Lett.* **2019**, *19*, 5176.
(24) Kulbak, M.; Cahen, D.; Hodes, G. How important is the organic part of lead halide perovskite photovoltaic cells? Efficient $CsPbBr_3$ cells. *J. Phys. Chem. Lett.* **2015**, *6*, 2452.
(25) Eperon, G. E.; Stranks, S. D.; Menelaou, C.; Johnston, M. B.; Herz, L. M.; Snaith, H. J. Formamidinium lead trihalide: a broadly tunable perovskite for efficient planar heterojunction solar cells. *Energy Environ. Sci.* **2014**, *7*, 982.
(26) Eperon, G. E.; Paterno, G. M.; Sutton, R. J.; Zampetti, A.; Haghighirad, A. A.; Cacialli, F.; Snaith, H. J. Inorganic cesium lead iodide perovskite solar cells. *J. Mater. Chem. A* **2015**, *3*, 19688.
(27) Zhao, D.; Yu, Y.; Wang, C. L.; Liao, W. Q.; Shrestha, N.; Grice, C. R.; Cimaroli, A. J.; Guan, L.; Ellingson, R. J.; Zhu, K.; Zhao, X. Z.; Xiong, R. G.; Yan, Y. F. Low-bandgap mixed tin-lead iodide perovskite absorbers with long carrier lifetimes for all-perovskite tandem solar cells. *Nat. Energy* **2017**, *2*, 17018.
(28) Mcmeekin, D. P.; Sadoughi, G.; Rehman, W.; Eperon, G. E.; Saliba, M.; Horantner, M. T.; Haghighirad, A.; Sakai, N.; Korte, L.; Rech, B.; Johnston, M. B.; Herz, L. M.; Snaith, H. J. A mixed-cation lead mixed-halide perovskite absorber for tandem solar cells. *Science* **2016**, *351*, 151.
(29) Bush, K. A.; Palmstrom, A. F.; Yu, Z. J.; Boccard, M.; Cheacharoen, R.; Mailoa, J. P.; McMeekin, D. P.; Hoye, R. L. Z.; Bailie, C. D.; Leijtens, T.; Peters, L. M.; Minichetti, M. C.; Rolston, N.; Prasanna, R.; Sofia, S.; Harwood, D.; Ma, W.; Moghadam, F.; Snaith, H. J.; Buonassisi, T.; Holman, Z. C.; Bent, S. F.; McGehee, M. D. 23.6%-efficient monolithic perovskite/silicon tandem solar cells with improved stability. *Nat. Energy* **2017**, *2*, 17009.
(30) Eperon, G. E.; Leijtens, T.; Bush, K. A.; Prasanna, R.; Green, T.; Wang, J. T.; McMeekin, D. P.; Volonakis, G.; Milot, R. L.; May, R.; Palmstrom, A.; Slotcavage, D. J.; Belisle, R. A.; Patel, J. B.; Parrott, E. S.; Sutton, R. J.; Ma, W.; Moghadam, F.; Conings, B.; Babayigit, A.; Boyen, H. G.; Bent, S.; Giustino, F.; Herz, L. M.; Johnston, M. B.; McGehee, M. D.; Snaith, H. J. Perovskite-perovskite tandem photovoltaics with optimized band gaps. *Science* **2016**, *354*, 861.
(31) Zhu, Z.; Zhao, D.; Chueh, C.-C.; Shi, X.; Li, Z.; Jen, A. K. Y. Highly efficient and stable perovskite solar cells enabled by all crosslinked charge-transporting layers. *Joule* **2018**, *2*, 168.
(32) Back, H.; Kim, G.; Kim, J.; Kong, J.; Kim, T. K.; Kang, H.; Kim, H.; Lee, J.; Lee, S.; Lee, K. Achieving long-term stable perovskite solar cells via ion neutralization. *Energy Environ. Sci.* **2016**, *9*, 1258.
(33) Wang, N.; Zhao, K.; Ding, T.; Liu, W.; Ahmed, A. S.; Wang, Z.; Tian, M.; Sun, X. W.; Zhang, Q. Improving interfacial charge recombination in planar heterojunction perovskite photovoltaics with small molecule as electron transport layer. *Adv. Energy Mater.* **2017**, *7*, 1700522.
(34) Gu, P.-Y.; Wang, N.; Wang, C.; Zhou, Y.; Long, G.; Tian, M.; Chen, W.; Sun, X. W.; Kanatzidis, M. G.; Zhang, Q. Pushing up the efficiency of planar perovskite solar cells to 18.2% with organic small molecules as the electron transport layer. *J. Mater. Chem. A* **2017**, *5*, 7339.
(35) Yao, K.; Leng, S. F.; Liu, Z. L.; Fei, L. F.; Chen, Y. J.; Li, S.; Zhou, N. G.; Zhang, J.; Xu, Y. X.; Zhou, L.; Huang, H. T.; Jen, A. K. -Y. Fullerene-anchored core-shell ZnO nanoparticles for efficient and stable dual-sensitized perovskite solar cells. *Joule* **2019**, *3*, 417.
(36) Ke, W.; Fang, G.; Liu, Q.; Xiong, L.; Qin, P.; Tao, H.; Wang, J.; Lei, H.; Li, B.; Wan, J.; Yang, G.; Yan, Y. Low-temperature solution-processed tin oxide as an alternative electron transporting layer for efficient perovskite solar cells. *J. Am. Chem. Soc.* **2015**, *137*, 6730.
(37) Tan, H.; Jain, A.; Voznyy, O.; Lan, X.; Garcia de Arquer, F. P.; Fan, J. Z.; Quintero-Bermudez, R.; Yuan, M.; Zhang, B.; Zhao, Y.; et al. Efficient and stable solution-processed planar perovskite solar cells via contact passivation. *Science* **2017**, *355*, 722.
(38) Zhang, H.; Cheng, J.; Lin, F.; He, H.; Mao, J.; Wong, K. S.; Jen, A. K. Y.; Choy, W. C. H. Pinhole-free and surfacenanostructured NiO_x film by room-temperature solution process for high-performance flexible perovskite solar cells with good stability and reproducibility. *ACS Nano* **2016**, *10*, 1503.
(39) He, Q.; Yao, K.; Wang, X.; Xia, X.; Leng, S.; Li, F. Room-temperature and solutionprocessable Cu-doped nickel oxide nanoparticles for efficient hole-transport layers of flexible large-area perovskite solar cells. *ACS Appl. Mater. Interfaces* **2017**, *9*, 41887.
(40) Xue, J.; Wang, R.; Chen, L.; Nuryyeva, S.; Han, T. H.; Huang, T.; Tan, S.; Zhu, J.; Wang, M.; Wang, Z. K.; Zhang, C.; Lee, J. W.; Yang, Y. A Small-Molecule "Charge Driver" enables Perovskite Quantum Dot Solar Cells with Efficiency Approaching 13%. *Adv. Mater.* **2019**, *31*, 1900111.
(41) Shin, S. S.; Yeom, E. J.; Yang, W. S.; Hur, S.; Kim, M. G.; Im, J.; Seo, J.; Noh, J. H.; Seok, S. I. Colloidally prepared La-doped $BaSnO_3$ electrodes for efficient, photostable perovskite solar cells. *Science* **2017**, *356*, 167.
(42) Chen, W.; Wu, Y.; Yue, Y.; Liu, J.; Zhang, W.; Yang, X.; Chen, H.; Bi, E.; Ashraful, I.; Gratzel, M.; et al. Efficient and stable large-area perovskite solar cells with inorganic charge extraction layers. *Science* **2015**, *350*, 944.
(43) Lou, Y.; Wang, Z. Aqueous-solution-processable metal oxides for high-performance organic and perovskite solar cells. *Nanoscale* **2017**, *9*, 13506.
(44) Look, D. C.; Reynolds, D. C.; Sizelove, J. R.; Jones, R. L.; Litton, C. W.; Cantwell, G.; Harsch, W. C. Electrical Properties of Bulk ZnO. *Solid State Commun.* **1998**, *105*, 399.
(45) Chen, S.; Small, C. E.; Amb, C. M.; Subbiah, J.; Lai, T. -h.; Tsang, S.-W.; Manders, J. R.; Reynolds, J. R.; So, F. Inverted polymer solar cells with reduced interface recombination. *Adv. Energy Mater.* **2012**, *2*, 1333.
(46) Brillson, L. J.; Mosbacker, H. L.; Hetzer, M. J.; Strzhemechny, Y.; Jessen, G. H.; Look, D. C.; Cantwell, G.; Zhang, J.; Song, J. J. Dominant effect of near-interface native point defects on ZnO Schottky barriers. *Appl. Phys. Lett.* **2007**, *90*, 102116.
(47) Yang, J.; Siempelkamp, B. D.; Mosconi, E.; De Angelis, F.; Kelly, T. L. Origin of the thermal instability in $CH_3NH_3PbI_3$ thin films deposited on ZnO. *Chem. Mater.* **2015**, *27*, 4229.
(48) Cheng, Y.; Yang, Q. D.; Xiao, J.; Xue, Q.; Li, H. W.; Guan, Z.; Yip, H. L.; Tsang, S. W. Decomposition of organometal halide perovskite films on zinc oxide nanoparticles. *ACS Appl. Mater. Interfaces* **2015**, *7*, 19986.
(49) Pacholski, C.; Kornowski, A.; Weller, H. Self-assembly of ZnO: from nanodots to nanorods. *Angew. Chem., Int. Ed.* **2002**, *41*, 1188.
(50) Zhang, Z. Y.; Shao, C. L.; Li, X. H.; Zhang, L.; Xue, H. M.; Wang, C. H.; Liu, Y. C. Electrospun nanofibers of ZnO-SnO_2 heterojunction with high photocatalytic activity. *J. Phys. Chem. C* **2010**, *114*, 7920.
(51) Wang, W. W.; Zhu, Y. J.; Yang, L. X. ZnO-SnO_2 hollow spheres and hierarchical nanosheets: hydrothermal preparation, formation mechanism, and photocatalytic properties. *Adv. Funct. Mater.* **2007**, *17*, 59.
(52) Zheng, L.; Zheng, Y.; Chen, C.; Zhan, Y.; Lin, X.; Zheng, Q.; Wei, K.; Zhu, J. Network structured SnO_2/ZnO heterojunction nanocatalyst with high photocatalytic activity. *Inorg. Chem.* **2009**, *48*, 1819.
(53) Meng, L.; Sun, C. K.; Wang, R.; Huang, W. C.; Zhao, Z. P.; Sun, P. Y.; Huang, T. Y.; Xue, J. J.; Lee, J. W.; Zhu, C. H.; Huang, Y.; Li, Y. F.; Yang, Y. Tailored phase conversion under conjugated polymer enables thermally stable perovskite solar cells with efficiency exceeding 21%. *J. Am. Chem. Soc.* **2018**, *140*, 17255.

DOI: 10.1021/jacs.9b06796
J. Am. Chem. Soc. 2019, 141, 17610−17616